RSC Advances

ROYAL SOCIETY OF CHEMISTRY

PAPER

View Article Online
View Journal | View Issue

Check for updates

Cite this: *RSC Adv.*, 2026, **16**, 8623

Hydrogen storage performance of $Ti_{0.75}Zr_{0.25}Mn_{0.9}CrFe_{0.1}$ alloy with different preparation methods

Yiqiang Mu,[a] Yanchen Zhou,[ab] Guo Yang,[b] Linhua Xu,[b] Huimin Xu,[b] Lixiao Zhu,[b] Xingbo Han,[b] Xinxin Chu,[b] Wei Liu[b] and Lijun Lv*[b]

Received 12th November 2025
Accepted 5th February 2026

DOI: 10.1039/d5ra08729e

rsc.li/rsc-advances

The $Ti_{0.75}Zr_{0.25}Mn_{0.9}CrFe_{0.1}$ alloy was prepared using both arc melting and magnetic levitation melting methods. Additionally, the arc-melted alloy was further processed by melt-spinning and annealing. The differences in microstructure and hydrogen storage performance among the alloys prepared were investigated. All these alloys exhibit a single C14-Laves phase structure. The alloys produced by arc-melting, annealing, and magnetic levitation-melting show distinct Zr element precipitation. In contrast, no evident element segregation was detected in the melt-spun alloy. The unit cell volume decreased in the order of: arc-melted (AM) > melt-spun (MS) > annealed (AN) > magnetic levitation-melted (ML) alloy. The plateau pressure of the alloys is: AM < MS < AN < ML. Compared with the AM, the maximum hydrogen storage capacity of the alloy formed by MS and AN is slightly reduced. Regarding hydrogen absorption kinetics, all four alloys reach saturation within 300 seconds. Compared to other preparation methods, melt-spinning can reduce the slope factor and hysteresis factor, and enhance its resistance to powdering.

1. Introduction

As the energy crisis continues to intensify and environmental problems worsen, the search for alternative clean energy sources has become an urgent priority.[1] Hydrogen has garnered significant attention due to its abundant reserves, high calorific value and pollution-free byproducts. However, safe, efficient storage and transportation remain critical challenges for its practical implementation and large-scale adoption.[2,3] Currently, there are three methods for hydrogen storage: high-pressure gas storage,[4] cryogenic liquid storage,[5] and metal hydrogen storage.[6] Compared to high-pressure gaseous and cryogenic liquid hydrogen storage, metal hydrogen storage offers distinct advantages, including enhanced safety and higher energy density.[7] Common hydrogen storage alloys include: rare earth-based hydrogen storage alloys, titanium-based hydrogen storage alloys, magnesium-based hydrogen storage alloys[8,9] and vanadium-based hydrogen storage alloys.[10] Compared to other types of hydrogen storage alloys, Ti–Mn based alloys offer several advantages, such as favorable activation performance, low cost, and rapid kinetics.[11] However, this type of alloy exhibits issues such as platform slope and hysteresis.[12] To ensure the alloy can be applied on a large scale, scholars have conducted extensive research on improving its hydrogen properties.

Element substitution is one of the methods for optimizing the hydrogen storage performance of hydrogen storage alloys. By replacing elements on either the A side or the B side, the hydrogen properties of the alloy can be enhanced.[13] Regarding substitution on the A side, Wu *et al.*[14] observed in their study of $Ti_{1-x}Ce_xV_{0.45}Mn_{1.5}$ ($x = 0, 0.05, 0.10, 0.15, 0.20$) alloys that the hysteresis factor first decreased and then increased with increasing Ce substitution, the minimum hysteresis factor was achieved when $x = 0.05$. Chen *et al.*[15] found in their study of Ti–V–Mn based alloys that substituting Zr for Ti increases the alloy's reversible hydrogen storage capacity, but both hysteresis factor and slope factor increase. Regarding substitution on the B side, Park *et al.*[16] found that reducing the stoichiometric ratio and incorporating V and Cu elements effectively decreased the platform slope factor. Ni *et al.*[17] demonstrated that when Mo replaced Mn, the hysteresis factor was decreased. When Fe replaced Mn, the hydrogen storage plateau were decreased. Zhang *et al.*[18] discovered that increasing the Mn/Cr ratio in $(Ti_{0.85}Zr_{0.15})_{1.02}Mn_yCr_{1.8-y}Fe_{0.2}$ ($y = 1.0$–0.4) alloy elevates both the hydrogen absorption plateau pressure and hysteresis factor. Qiao *et al.*[19] discovered in their study of the $Ti_{0.8}Zr_{0.2}Mn_{0.92}Cr_{0.87}Fe_{0.21}$ alloy that doping with Cu powder at different weight ratios (0, 3, 5, and 8 wt%) improved the alloy's hydrogen storage capacity and reduced the hysteresis factor.

The preparation method is one of the key approaches to altering the hydrogen storage performance of hydrogen storage

---

[a] *College of Civil Aviation, Shenyang Aerospace University, Shenyang, 110136, China*

[b] *Shanghai Institute of Applied Physics, Chinese Academy of Sciences, Shanghai 201800, China. E-mail: lvlijun@sinap.ac.cn*

alloys. Fan *et al.*[20] prepared $Ti_{0.85}Zr_{0.25}Mn_{1.5}V_{0.5}Fe_{0.1}$ alloy and revealed that annealing the as-cast alloy reduced the hysteresis factor and enhanced the reversible hydrogen storage capacity. Huang *et al.*[21] revealed that $TiCr_{1.1}V_{0.5}Fe_{0.1}Mn_{0.1}$ alloy to melt-spinning process and the hydrogen storage capacity of the alloy increased, but the hysteresis factor increase. In this paper, preliminary research by the team demonstrated that $Ti_{0.75}Zr_{0.25}Mn_{0.9}CrFe_{0.1}$ alloy exhibits high hydrogen storage capacity and excellent kinetic properties. To further improve the hydrogen properties of the alloy, The $Ti_{0.75}Zr_{0.25}Mn_{0.9}CrFe_{0.1}$ alloy was melted using both arc melting and magnetic levitation melting. Annealing and melt-spinning were applied to the arc-melted alloys. The effects of different preparation methods on the microstructure and hydrogen storage properties of the $Ti_{0.75}Zr_{0.25}Mn_{0.9}CrFe_{0.1}$ alloy were systematically investigated.

2. Experimental

2.1. Alloy preparation

The $Ti_{0.75}Zr_{0.25}Mn_{0.9}CrFe_{0.1}$ alloy was prepared by arc melting and magnetic levitation melting methods. The materials used (Ti, Zr, Mn, Cr, Fe) have a purity greater than 99.9%. To ensure homogeneity, the arc-melted alloy (AM) was turned over and remelted three times, the magnetic levitation melted alloy (ML) was likewise turned over and remelted three times. In order to remove oxide scales, the alloy was mechanically polished using sandpaper. The alloy is broken into small pieces and placed in a glove box to maintain the reliability of subsequent experiments and testings.

A 20 g alloy, prepared by arc melting, was placed into the melt-spinning furnace and processed at a wheel speed of 800 $m\ min^{-1}$(MS). A 20 g alloy, prepared by arc melting, was sealed in a quartz glass tube filled with argon and annealed at 1085 K for 5 h(AN), then cooled with the furnace set to 30 °C and removed.

2.2. Structural characterization

The phase structure of the alloys was collected by X-ray diffraction (XRD) from Bruker. Measurements were performed in continuous scan mode with 2θ range from 20° to 80° at a scan rate of 1.5° per minute. Rietveld refinement of the XRD pattern was carried out using TOPAS software to analyze the phase composition and crystal structure information of the alloys. The surface morphology of the alloy was observed using Merlin compact scanning electron microscope (SEM) and the distribution of alloying elements was analyzed by energy dispersive spectroscopy (EDS).

The amount of alloy powder was dispersed in deionized water and subjected to ultrasonic agitation for 10 minutes to achieve suitable and stable obscuration. The particle size distribution was measured using a laser particle size analyzer (Malvern Mastersizer 2000). The measurement was repeated five times and the average value was calculated.

2.3. Hydrogen storage properties

The pressure–composition–temperature (*P*–*C*–*T*) curves were measured with a Sieverts-type apparatus.[22,23] The alloy ingots were mechanically crushed into powder, and the 1.5 g samples powder was loaded into the reactor. In order to remove surface impurities adhered to the alloy powder, the reactor was evacuated for 40 min at 303 K and activated upon 7 MPa hydrogen absorption/desorption cycles. Following alloy activation, the PCT and kinetic testing were conducted at 303 K, 318 K, and 333 K. The maximum pressure were both set at 7 MPa.

3. Results and discussion

3.1. Structural analysis

Fig. 1 present the XRD patterns of the $Ti_{0.75}Zr_{0.25}Mn_{0.9}CrFe_{0.1}$ alloys prepared by different methods. The results reveal that all alloys exhibit a single-phase structure. Comparison with PDF card #04-005-189 confirms this phase to be the C14 Laves phase (space group $P6_3/mmc$). This result is consistent with that reported by Ni *et al.*[17].

Fig. 1(b) presents a magnified view of the XRD patterns in the 42–45° range for the alloys prepared by different methods. Compared to the arc-melted alloy, the XRD peak positions of the magnetic levitation melting alloy, the annealed and melt-spun alloy shifted to the right. Pan *et al.*[24] observed that,in their study on $Ti_{0.84}Zr_{0.16}Mn_{0.9}Cr_{0.7+x}Fe_{0.1}$ ($x = 0, 0.1, 0.2$) alloys, the

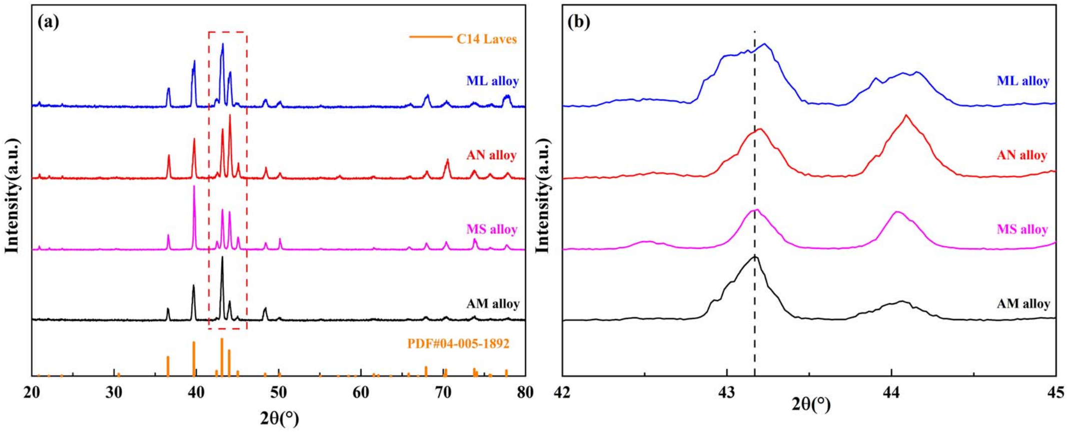

Fig. 1 (a) XRD patterns of $Ti_{0.75}Zr_{0.25}Mn_{0.9}CrFe_{0.1}$ alloy samples prepared by different technique; (b) zoom of (a) in the 2θ range of 42–45°.

Table 1 Lattice parameters of $Ti_{0.75}Zr_{0.25}Mn_{0.9}CrFe_{0.1}$ alloy samples prepared by different technique

Preparation method	a/Å	c/Å	a/c	V Å^{-3}	Strain(%)	FWHM	GOF
AM	4.9139	8.0676	0.6090	168.766	0.25	0.249	1.43
MS	4.9215	8.0535	0.6111	168.684	0.14	0.219	1.73
AN	4.9166	8.0590	0.6100	168.421	0.31	0.260	1.60
ML	4.9138	8.0646	0.6093	168.389	0.40	0.381	1.92

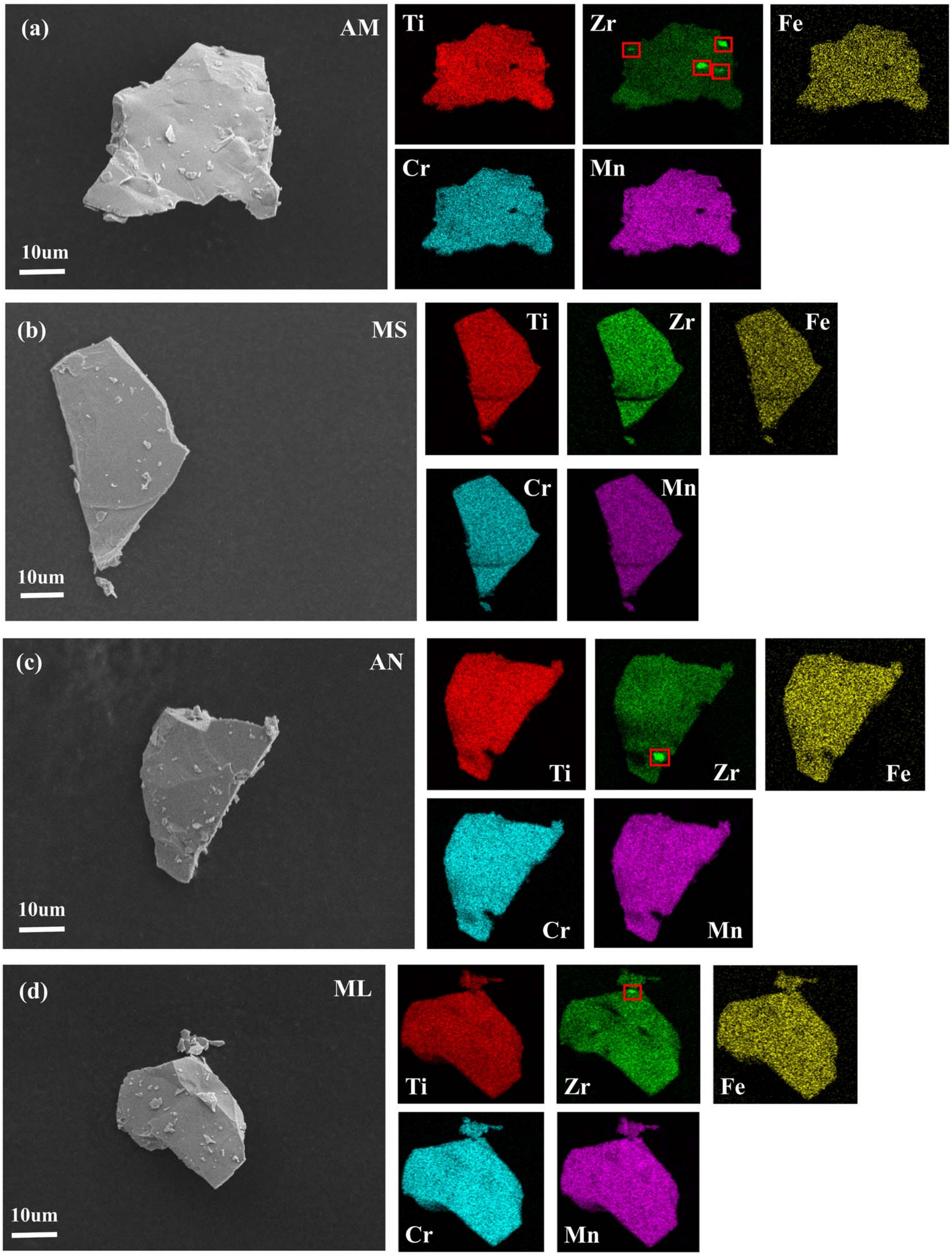

Fig. 2 SEM images and EDS mapping of $Ti_{0.75}Zr_{0.25}Mn_{0.9}CrFe_{0.1}$ alloy samples prepared by different technique: (a) arc melted, (b) melt-spun, (c) annealed, (d) magnetic levitation melted.

peak position of the XRD pattern shifted to the right and the unit cell volume decreased, this consistent with the findings in this study. Among these alloys, the intensity of the diffraction peak of the melt-spun alloy is the highest. This indicates that the crystallinity of the alloy is the highest. To further investigate the lattice parameters and unit cell volume, Rietveld refinement was performed based on the Bragg equation.

$$2d\sin\theta = n\lambda \tag{1}$$

The XRD patterns were refined with TOPAS software and the resulting unit cell parameters are listed in Table 1; All results showed GOF (Goodness of Fit) value of less than 2, indicating the reliability of the refinement data. The results in Table 1 show that the unit cell volume gradually decreases in the order of AM > MS > AN > ML. The unit cell of $Ti_{0.75}Zr_{0.25}Mn_{0.9}CrFe_{0.1}$ alloy was changed after annealing and melt-spinning treatment. Cheng *et al.*[25] studied the effect of annealing temperature on the hydrogen storage properties of TiZrCrMnFeNi alloy, and found that different annealing temperatures had different effects on the unit cell volume of TiZrCrMnFeNi alloy. This is because the unit cell volume of C14 Laves phase is greatly affected by the annealing temperature, and the annealing temperature directly regulates the lattice parameters of C14 phase. Huang *et al.*[26] studied the effect of annealing on the structure and hydrogen absorption/desorption characteristics of $La_{0.78}Mg_{0.22}Ni_{3.48}Co_{0.22}Cu_{0.12}$ alloy. It was found that annealing treatment can make the unit cell volume of $La_{0.78}Mg_{0.22}Ni_{3.48}Co_{0.22}Cu_{0.12}$ alloy smaller. The microstructure change of the alloy during annealing is affected by annealing temperature and alloy composition. Therefore, the decrease of unit cell parameters may be caused by the annihilation of lattice strain and crystal defects during annealing. Therefore, in this study, the cell volume of the alloy after melt-spinning and annealing treatment becomes smaller, which may be caused by the lattice strain and the annihilation of crystal defects during the process. The melt-spun alloy exhibits significantly reduced lattice strain, which is attributed to the enhanced crystallinity, elimination of crystal defects, and release of internal stress during the rapid solidification process.[20]

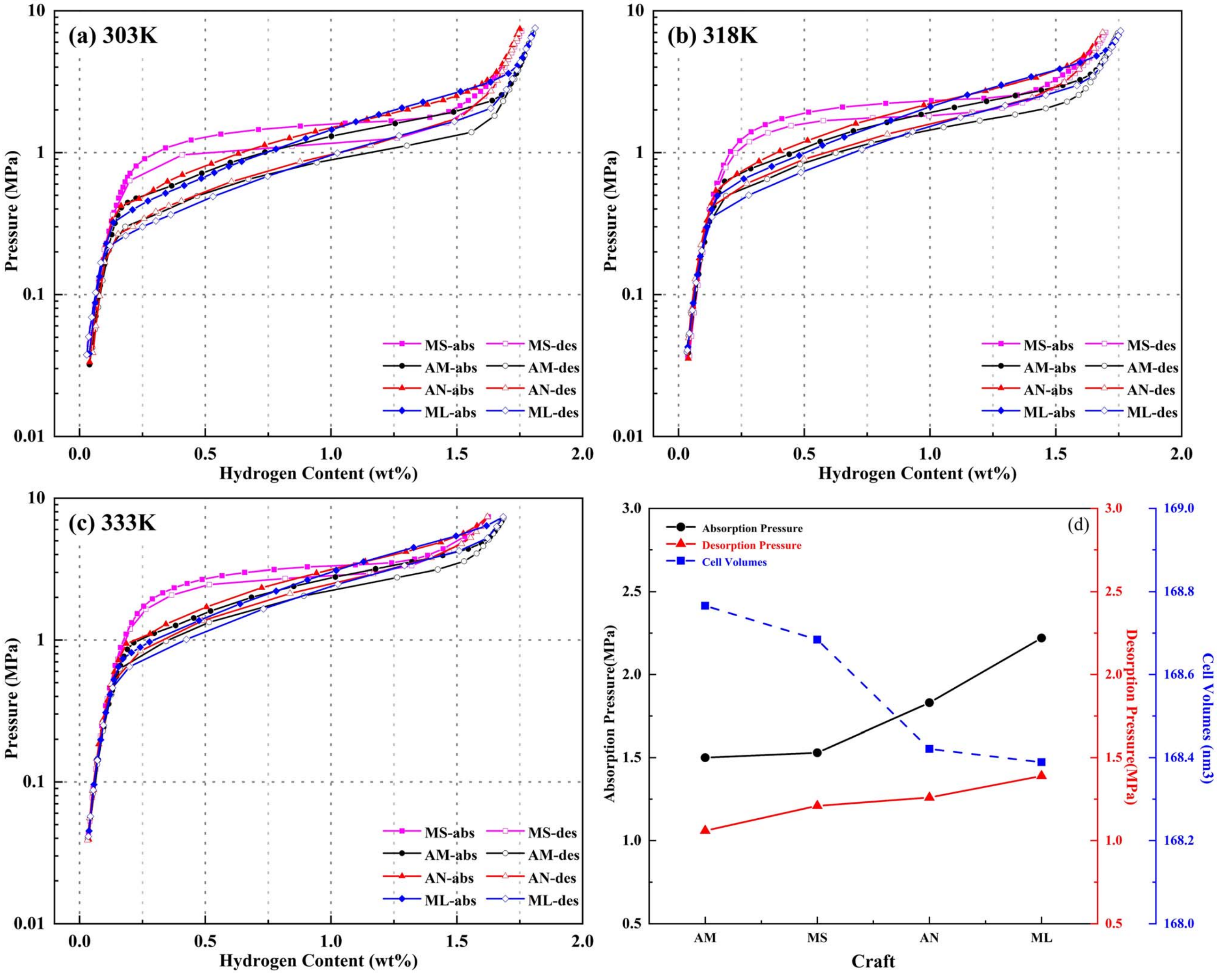

Fig. 3 *P*–*C*–*T* curves of the $Ti_{0.75}Zr_{0.25}Mn_{0.9}CrFe_{0.1}$ alloy samples prepared by different technique: (a) 303 K, (b) 318 K, (c) 333 K, (d) the plateau pressure and cell volumes of the $Ti_{0.75}Zr_{0.25}Mn_{0.9}CrFe_{0.1}$ alloy samples prepared by different technique.

The surface morphology and element distribution of the alloys are analyzed by SEM with EDS mapping. The scanning electron microscopy (SEM) and energy dispersive spectroscopy (EDS) of the $Ti_{0.75}Zr_{0.25}Mn_{0.9}CrFe_{0.1}$ before hydrogen absorption shown in Fig. 2. On the EDS diagram, Ti, Zr, Mn, Cr and Fe are shown as red, green, bright red, blue and yellow. The arc-melted, annealed and magnetic levitation melted alloys all exhibit pronounced Zr segregation. This may be attributed to the absence of rapid cooling during their solidification, which facilitated the element's precipitation.[27]

3.2. Hydrogen storage properties

Fig. 3 shows the *PCT* curves of the $Ti_{0.75}Zr_{0.25}Mn_{0.9}CrFe_{0.1}$ alloys prepared by different methods at 303 K, 318 K, and 333 K under a maximum hydrogen pressure of 7 MPa. Table 2 presents the hydrogen storage performances of these alloys. It can be seen that the arc-melted and magnetic levitation melted alloys exhibit identical maximum hydrogen capacities at 303 K, 318 K and 333 K. But the melt-spun and annealed alloys display a slight decrease in maximum hydrogen storage capacity. Generally, the hydrogen storage capacity of metal hydrides is affected by many factors, including the interstitial cell size.[28] When the cell volume of the alloy becomes larger, the interstitial cell size becomes larger, resulting in an increase in the hydrogen storage capacity of the alloy.[29] Through the lattice parameters of $Ti_{0.75}Zr_{0.25}Mn_{0.9}CrFe_{0.1}$ alloys prepared by different methods, it can be seen that the cell volume of the alloy decreases after the melt-spinning and annealing treatment, so the maximum hydrogen storage capacity decreases.

At 303 K, the plateau pressure increases from 1.50 MPa (AM) to 2.22 MPa (ML). The order of hydrogen adsorption plateau pressures is: AM < MS < AN < ML. Lundin *et al.*[30] notes that larger unit cell volume facilitates the penetration of hydrogen atoms into the lattice interstices. This results in a decrease in the plateau pressure. Fig. 3(d) shows the relationship between the absorption plateau pressure and unit-cell volume of $Ti_{0.75}Zr_{0.25}Mn_{0.9}CrFe_{0.1}$ alloys prepared by different methods at 303 K. It can be seen that the hydrogen absorption plateau pressure is inversely proportional to the unit cell volume. The trend in plateau pressure aligns with the interstitial size effect proposed by Lundin *et al.*[30] An increase in unit cell volume expands the interstitial hole size. This enhances hydride stability and reduces the strain energy during hydrogen occupation. Consequently, the hydrogen absorption plateau pressure decreases.

Hysteresis factor is defined as $H_f = \ln(P_{abs}/P_{des})$. The hysteresis factors for $Ti_{0.75}Zr_{0.25}Mn_{0.9}CrFe_{0.1}$ alloys prepared by different methods at various temperatures were calculated and are presented in Table 2. The Table 2 shows that compared to the arc-melted alloy, the hysteresis factor decreases for the melt-spun alloy, while it increases for the annealed and magnetic levitation melted alloys. This indicates that melt-spinning progress can reduce the hysteresis factor. Hysteresis factor correlates with lattice strain in metal hydrides.[31] Park *et al.*[16] found that lattice strain can be represented by the full width at half maximum (FWHM) of the main peak in the XRD diffraction spectrum. A large FWHM value indicates increase the degree of variation in the lattice distortion and grow the hysteresis factor. Fig. 4 shows that FWHM value with the hysteresis factor for $Ti_{0.75}Zr_{0.25}Mn_{0.9}CrFe_{0.1}$ alloys prepared by different methods. Higher FWHM indicates greater lattice strain and larger hysteresis. Ni *et al.*[17] reported the same trend for $Ti_{0.9}Zr_{0.1}Mn_{0.95}Cr_{0.7}V_{0.2}M_{0.15}$ (M = Fe, Co, Ni, Cu, Mo) alloys, confirming our findings.

The slope factor is used to determine the degree of disorder in metal hydrides. It an inherent property of metal hydrides.[32] It is defined as Slope = $\ln(P_{75\%}/P_{15\%})$, with $P_{75\%}$ and $P_{15\%}$ the plateau pressures at 75 wt% and 15 wt% of total capacity. Table 2 shows that the magnetic levitation melted alloy has the steepest plateau slope, whereas the melt-spun alloy exhibits the smallest. Park *et al.*[33] found that the cause of hydrogen absorption platform tilting is the inhomogeneit of alloy composition. The heterogeneous composition results in

Table 2 *P–C–T* performance of the $Ti_{0.75}Zr_{0.25}Mn_{0.9}CrFe_{0.1}$ alloy samples prepared by different technique[a,b,c,d,e]

Preparation method	*T*/K	P_{abs}/MPa	P_{des}/MPa	H_f	S_f	C_{max}/wt%
AM	303	1.50	1.06	0.34	1.24	1.80
	318	2.22	1.67	0.28	1.21	1.75
	333	2.88	2.34	0.21	1.19	1.69
MS	303	1.53	1.21	0.24	0.64	1.76
	318	2.33	1.90	0.20	0.68	1.70
	333	3.05	2.74	0.11	0.75	1.63
AN	303	1.83	1.28	0.36	1.40	1.75
	318	2.68	1.95	0.32	1.35	1.67
	333	3.67	2.92	0.23	1.31	1.62
ML	303	2.22	1.32	0.51	1.59	1.80
	318	2.90	2.02	0.36	1.55	1.75
	333	4.05	2.94	0.32	1.50	1.69

[a] P_{abs} is the hydrogen absorption plateau pressure in PCT curves at the corresponding temperatures. [b] P_{des} is the hydrogen desorption plateau pressure in PCT curves at the corresponding temperatures. [c] H_f is the equilibrium pressure hysteresis factor ($H_f = \ln(P_{abs}/P_{des})$). [d] S_f is the hydrogen absorption equilibrium pressure slope factor ($S_f = \ln(P_{75\%}/P_{15\%})$). [e] C_{max} is the maximum hydrogen storage capacity.

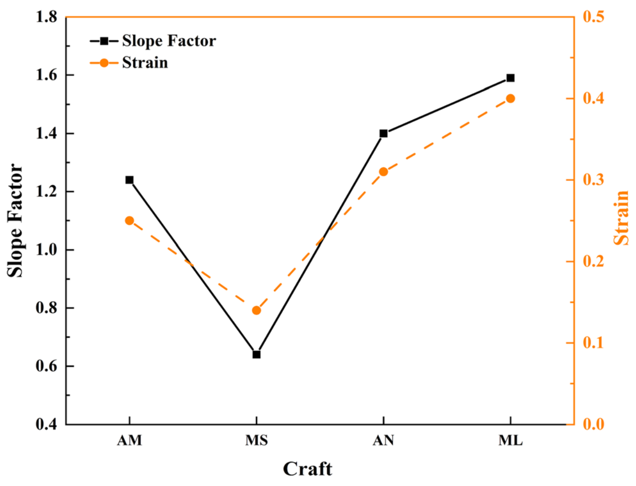

Fig. 4 Relationship between the hysteresis factor and FWHM value.

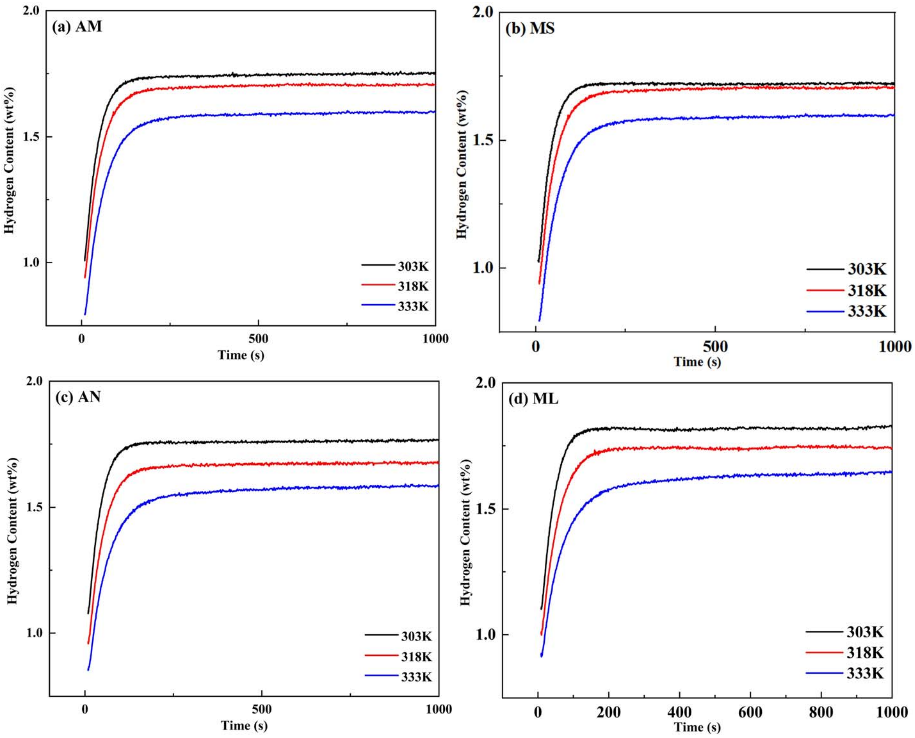

Fig. 5 Kinetic curves: (a) arc-melted alloy (b) melt-spun alloy (c) annealed alloy (d) magnetic levitation-melted alloy.

variations of the elemental environment adjacent to the interstitial sites occupied by hydrogen atoms. This leads to changes in the interstitial binding energy, which subsequently increases the slope factor. Fig. 2 reveals the homogeneous distribution of Zr in the melt-spun alloy and Zr segregation is observed in alloys prepared by other methods. Therefore, the melt-spinning process promotes a more homogeneous elemental distribution, thus reducing the plateau slope of the alloy.

3.3. Hydrogen absorption kinetics performance

Fig. 5 shows the hydrogen absorption kinetics curves of $Ti_{0.75}Zr_{0.25}Mn_{0.9}CrFe_{0.1}$ alloys prepared by different methods at 303 K, 318 K and 333 K. It can be seen from Fig. 5 that under the same preparation method, as the temperature increases, the hydrogen storage capacity of the alloy gradually decreases and the hydrogen absorption rate becomes slower. Under the condition of the same maximum hydrogen pressure, the hydrogen absorption plateau pressure of the alloy gradually increases with the increasing of temperature and the pressure driving force decreases with the increase of the hydrogen absorption plateau pressure. The hydrogen absorption rate increases with the increase of pressure driving force. Therefore, under the same preparation method, the hydrogen absorption rate of the alloy slows down with the increase of temperature.

The Chou model was used to analyze the kinetics of the alloys.[34] The expression of the Chou model is as follows:

$$\xi_{d} = 1 - \left[1 - \sqrt{\frac{t}{t_{c(d)}}}\right]^{3} \qquad (2)$$

Fig. 6 is the hydrogen absorption kinetics normalized curve of $Ti_{0.75}Zr_{0.25}Mn_{0.9}CrFe_{0.1}$ alloy prepared by different methods at 333 K. It can be seen from Fig. 6 that all alloys can reach the maximum hydrogen absorption capacity within 300 s, showing good hydrogen absorption kinetics. The $t_{90\%}$ is the time required for $Ti_{0.75}Zr_{0.25}Mn_{0.9}CrFe_{0.1}$ alloy with different preparation methods to reach 90% hydrogen storage capacity at 333 K. From Fig. 6, it can be seen that the $t_{90\%}$ of the alloy from large to small is: ML > AN > MS > AM. Fig. 7 shows the kinetic fitting

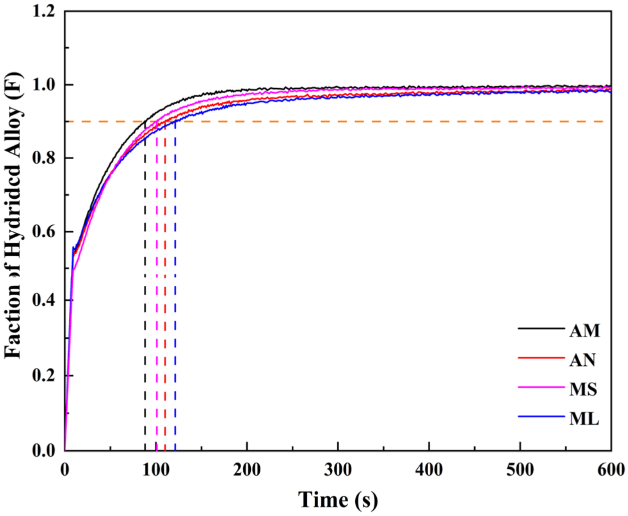

Fig. 6 Kinetic normalized curves of $Ti_{0.75}Zr_{0.25}Mn_{0.9}CrFe_{0.1}$ alloy samples prepared by different methods at 333 K.

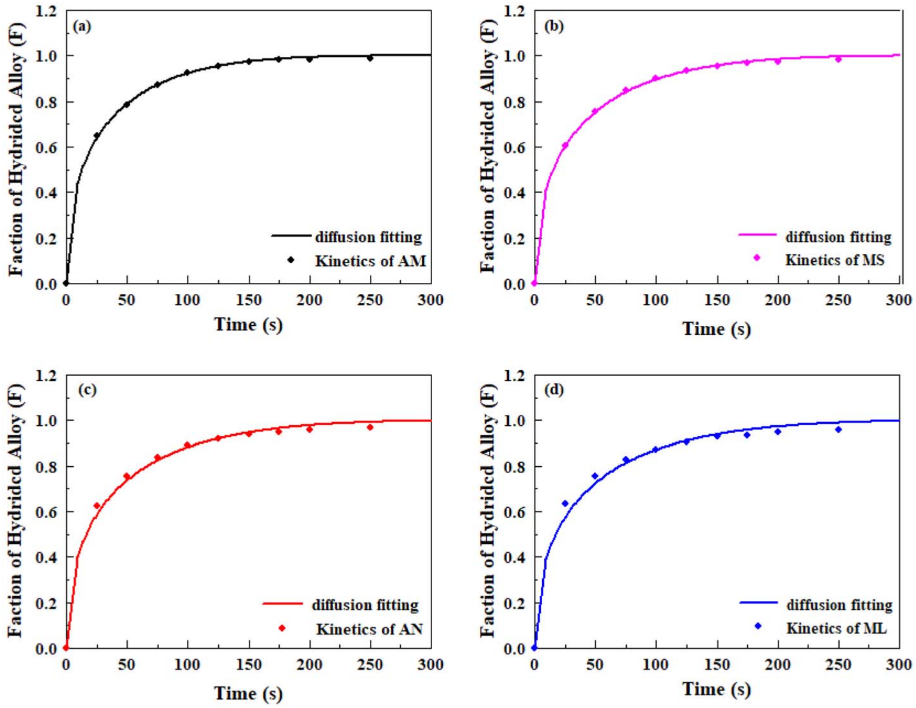

Fig. 7 The fitted hydrogen absorption kinetic curves of the $Ti_{0.75}Zr_{0.25}Mn_{0.9}CrFe_{0.1}$ alloy: (a) arc-melted alloy (b) melt-spun alloy (c) annealed alloy (d) magnetic levitation-melted alloy.

diagram of Chou model of hydrogen absorption kinetics of $Ti_{0.75}Zr_{0.25}Mn_{0.9}CrFe_{0.1}$ alloy prepared by different methods at 333 K. The fitting results are in good agreement with the experimental results, indicating that the control step of hydrogen absorption kinetics of $Ti_{0.75}Zr_{0.25}Mn_{0.9}CrFe_{0.1}$ alloy prepared by different methods is the diffusion control of hydrogen atoms in metal hydrides. Jiang *et al.*[35] found that the hydrogen absorption rate of the alloy is inversely proportional to the plateau pressure and proportional to the diffusion coefficient of hydrogen in the metal through the kinetic model. Under the same initial hydrogen pressure, the higher the hydrogen absorption platform pressure, the smaller the pressure difference, the smaller the driving force, and the slower the hydrogen absorption rate. It can be seen from the previous text that the order of hydrogen absorption plateau pressure of $Ti_{0.75}Zr_{0.25}Mn_{0.9}CrFe_{0.1}$ alloy under different preparation methods is: ML > AN > MS > AM. Therefore, the order of hydrogen absorption rate of $Ti_{0.75}Zr_{0.25}Mn_{0.9}CrFe_{0.1}$ alloy under different preparation methods is: AM > MS > AN > ML.

3.4. Thermodynamic properties

To study the thermodynamic properties of $Ti_{0.75}Zr_{0.25}Mn_{0.9}CrFe_{0.1}$ alloys prepared by different methods. Fig. 8 show that Van't Hoff curves were plotted using PCT curves at various temperatures. All curves had fitting coefficients (R^2) above 0.99, indicating reliable results. Table 3 show that thermodynamic parameters.

The Table 3 shows that the enthalpy change for hydrogen adsorption ranges from 18 to 20 KJ mol^{-1}, while that for

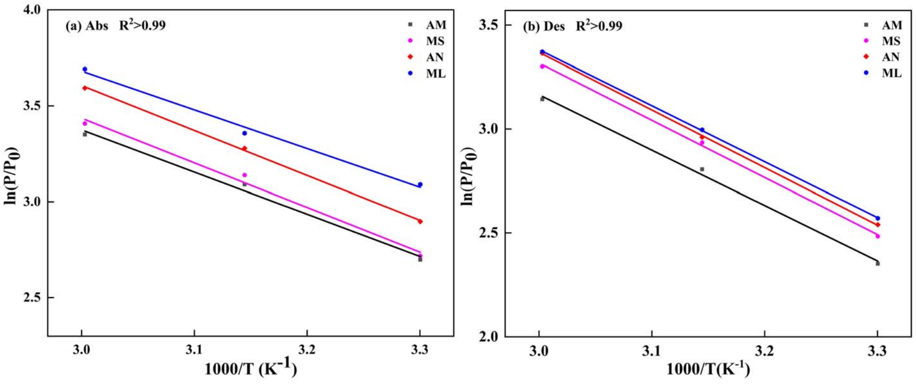

Fig. 8 Van't Hoff curves of the $Ti_{0.75}Zr_{0.25}Mn_{0.9}CrFe_{0.1}$ alloy samples prepared by different methods. (a) absorption, (b) desorption.

Table 3 Thermodynamic properties of the $Ti_{0.75}Zr_{0.25}Mn_{0.9}CrFe_{0.1}$ alloy samples prepared by different methods at 303 K

Preparation method	ΔH_{abs}/KJ mol^{-1}	ΔH_{des}/KJ mol^{-1}	ΔS_{abs}/J mol^{-1} K^{-1}	ΔS_{des}/J mol^{-1} K^{-1}
AM	−19.9	23.5	−88.0	96.9
MS	−19.3	23.3	−87.4	96.2
AN	−18.9	23.1	−86.7	96.1
ML	−18.3	22.6	−85.7	95.9

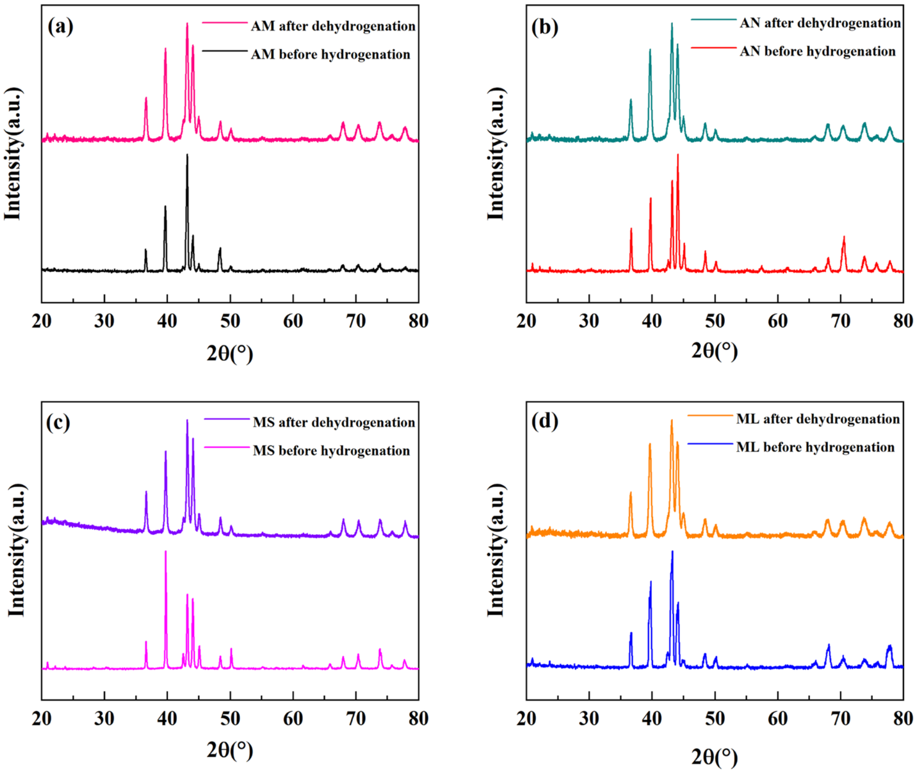

Fig. 9 XRD patterns of $Ti_{0.75}Zr_{0.25}Mn_{0.9}CrFe_{0.1}$alloy prepared by different methods before and after hydrogen absorption/desorption: (a) arc-melted alloy (b) melt-spun alloy (c) annealed alloy (d) magnetic levitation-melted alloy.

hydrogen desorption ranges from 22 to 24 KJ mol^{-1}. The absolute values of enthalpy changes for hydrogen adsorption and desorption follow the order AM > MS > AN > ML. This result aligns with the trend in unit cell volume changes. It indicates a correlation between unit cell volume and enthalpy change. Li *et al.*[36] proposed that the formation enthalpies of hydrides depends on two factors: the electronegativity factor and the electron density parameter. The electron density parameter is associated with the molar volume. Due to these dependencies, the enthalpy is proportional to the unit cell volume. In the present study, as the unit cell volume of the alloy decreases, the hydride formation enthalpy also decreases. This conclusion is supported by the studies of Cao *et al.*[37]

3.5 Hydrogen cycling properties

In order to analyze the phase structure, we performed XRD characterization of the alloys prepared by different methods after hydrogen absorption/desorption (Fig. 9). It can be seen from Fig. 9 that the alloy after hydrogen absorption/dehydrogenation maintains the original phase composition (C14 Laves phase) and no other phases are formed. Notably, the peaks of the alloy after hydrogen absorption/dehydrogenation exhibit significant broadening, which may be attributed to increased microstrain, crystallite refinementor even amorphization effects.[38]

Fig. 10 shows SEM images of the $Ti_{0.75}Zr_{0.25}Mn_{0.9}CrFe_{0.1}$ alloy samples prepared by different methods after experiments. The results reveal that all four alloys exhibit significant surface cracks on the particles after experiments. Akash Verma *et al.*[39] found that when preparing NaCl microcrystals, the grains were repeatedly applied pressure and there would be dislocations inside. The accumulation of dislocations would make the grains become smaller subgrains. In the hydrogen storage alloy, hydrogen atoms enter and exit the crystal structure, resulting in lattice stress. These lattice stresses lead to the generation of lattice defects, which in turn produces lattice strain, making the particles break into smaller particles. Therefore, there were many cracks in the particles. Fig. 11 shows the particle size distribution curve of $Ti_{0.75}Zr_{0.25}Mn_{0.9}CrFe_{0.1}$ alloy after hydrogen absorption and

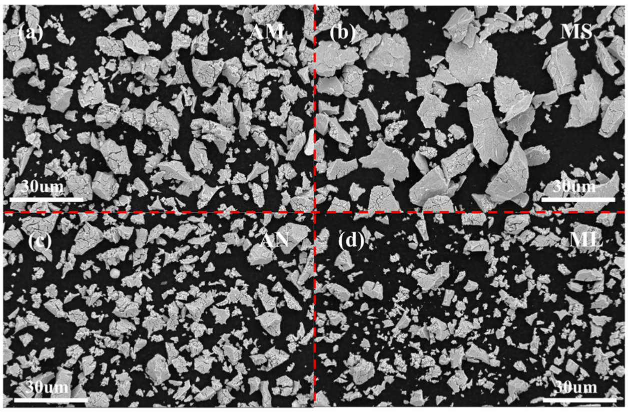

Fig. 10 SEM images of different status of $Ti_{0.75}Zr_{0.25}Mn_{0.9}CrFe_{0.1}$ alloy samples after experiment. (a) arc-melted; (b) melt-spun; (c) annealed; (d) magnetic levitation melted.

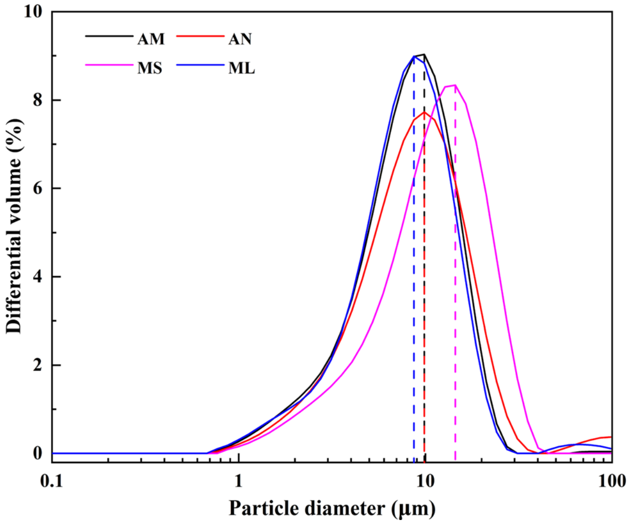

Fig. 11 Particle size distribution curves of $Ti_{0.75}Zr_{0.25}Mn_{0.9}CrFe_{0.1}$ alloy after experiment.

desorption under different preparation methods. The particle size data of the alloy powders are shown in Table 4. It can be seen that the particle size of MS is larger than that of the other alloys. The other three alloys result in similar. K. Young *et al.*[40] showed that the *a*/*c* ratio is related to the pulverization resistance. A higher *a*/*c* value corresponds to improved resistance to pulverization. As can be seen from Table 1, the MS exhibits a larger *a*/*c* ratio compared to the other three alloys. The particle size remains larger. Therefore, the melt-spinning progress can increase the pulverization resistance of alloys.

Table 4 Detailed powder size information of the $Ti_{0.75}Zr_{0.25}Mn_{0.9}CrFe_{0.1}$ alloy samples after experiment[a]

	Power size (μm)			
Preparation method	D_{10}	D_{50}	D_{90}	D_a
AM	3.364	8.725	16.494	8.958
MS	4.214	12.471	25.012	12.444
AN	3.161	8.542	20.330	9.371
ML	3.426	8.627	17.049	9.080

[a] D_a is the average particle size of the alloy particles in the range of 0–100 μm.

4. Conclusion

The $Ti_{0.75}Zr_{0.25}Mn_{0.9}CrFe_{0.1}$ alloys were prepared by four different methods: arc melting, melt spinning, annealing and magnetic levitation melting. The microstructure and hydrogen absorption/desorption properties of the alloys were systematically studied. The following main conclusions can be drawn from the results and analysis of this study:

(1) The alloy under the four processes maintains a single C14 Laves phase structure and the cell volume of the four processes is in the order of AM > MS > AN > ML.

(2) The plateau pressure of the alloy is: AM < MS < AN < ML. Compared with the AM, the maximum hydrogen storage capacity of the alloy treated by MS and AN is slightly reduced. The MS can effectively improve the hysteresis and slope of the alloy. At 303 K, all alloys can reach the hydrogen absorption saturation of the alloy within 300 s, showing good hydrogen absorption kinetics.

(3) Among the four preparation methods, the melt-spinning progress can improve the hysteresis factor and slope factor of $Ti_{0.75}Zr_{0.}25Mn0_{.9}CrFe_{0.1}$ alloy, and improve the pulverization resistance of the alloy.

Author contributions

Yiqiang Mu did the resource, investigation and investigation. Yanchen Zhou did the writing – original draft, writing – review and editing, validation, investigation and formal analysis. Guo Yang did the data curation and methodology. Linhua Xu did the software. Huimin Xu did the project administration, formal analysis and funding acquisition. Lixiao Zhu did the formal analysis and supervision. Xingbo Han did conceptualization and visualization. Xinxin Chu did the validation and supervision. Wei Liu did the formal analysis. Lijun Lv did the supervision and funding acquisition.

Conflicts of interest

The authors declare that they have no known competing financial interests or personal relationships that could have appeared to influence the work reported in this paper.

Data availability

All data included in this study are available upon request by contacting the corresponding author.

Acknowledgements

This work was supported by the National Natural Science Foundation of China (No. 12305407)

References

1 J. O. Abe, A. P. I. Popoola, E. Ajenifuja and O. M. Popoola, *Int. J. Hydrogen Energy*, 2019, **44**, 15072–15086.

2 M. Yang, R. Hunger, S. Berrettoni, B. Sprecher and B. Wang, *Clean Energy*, 2023, **7**, 190–216.

3 A. M. Abdalla, S. Hossain, O. B. Nisfindy, A. T. Azad, M. Dawood and A. K. Azad, *Energy Convers. Manage.*, 2018, **165**, 602–627.

4 M. R. Usman, *Renewable Sustainable Energy Rev.*, 2022, **167**, 112743.

5 M. Aziz, *Energies*, 2021, **14**, 5917.

6 T. Qureshi, M. M. Khan and H. S. Pali, *J. Alloys Compd.*, 2024, **1004**, 175668.

7 S. Niaz, T. Manzoor and A. H. Pandith, *Renewable Sustainable Energy Rev.*, 2015, **50**, 457–469.

8 P. Xiao, J. Liu, D. Guo, L. Yang, L. Sun, S. Li, L. Xu and H. Liu, *J. Alloys Compd.*, 2023, **955**, 170297.

9 L. Sun, R. Sun, J. Liu, M. Zhu, X. Zhang, D. Guo, K. Yin, Z. Zhuang, X. Zhu and P. Xiao, *Nanoscale*, 2024, **16**, 19873–19880.

10 N. Klopčič, I. Grimmer, F. Winkler, M. Sartory and A. Trattner, *J. Alloys Compd.*, 2023, **72**, 108456.

11 N. A. A. Rusman and M. Dahari, *Int. J. Hydrogen Energy*, 2016, **41**, 12108–12126.

12 A. Boretti, *Next Res.*, 2025, **2**, 100226.

13 J. Tu, P. Zhou, S. Chen, S. Shen, X. Liu, X. Xiao, Z. Li and L. Ouyang, *Mater. Sci. Eng. R Rep.*, 2026, **167**, 101089.

14 R. Wu, X. Zhao, D. Ke, J. Liu, F. Hu, R. Li, S. Zou and B. Zhang, *J. Alloys Compd.*, 2024, **976**, 173163.

15 X. Y. Chen, R. R. Chen, X. Ding, H. Z. Fang, X. Z. Li, H. S. Ding, Y. Q. Su, J. J. Guo and H. Z. Fu, *Energy*, 2019, **166**, 587–597.

16 J.-G. Park, H.-Y. Jang, S.-C. Han, P. S. Lee and J.-Y. Lee, *J. Alloys Compd.*, 2001, **325**, 293–298.

17 B. Ni, J. Zhu, G. Yang, L. Xu, H. Leng, W. Liu, T. Pan, X. Han and L. Lv, *Prog. Nat. Sci. Mater.*, 2024, **34**, 304–313.

18 X. Zhang, B. Li, L. Wang, W. Xiong, J. Li, S. Zhou, J. Xu, Y. Zhao, X. He and H. Yan, *Int. J. Hydrogen Energy*, 2024, **51**, 193–201.

19 W. Qiao, D. Yin, S. Zhao, N. Ding, L. Liang, C. Wang, L. Wang, M. He and Y. Cheng, *Chem. Eng. J.*, 2023, **465**, 142837.

20 C. Fan, B. Zhao, L. Ji, Y. Li, W. Wang, L. Zhang and S. Han, *J. Alloys Compd.*, 2025, **1014**, 178839.

21 T. Huang, Z. Wu, S. Feng, B. Xia and N. Xu, *Mater. Sci. Eng., A.*, 2005, **390**, 362–365.

22 H. H. Cheng, W. B. Li, W. Chen, D. M. Chen, M. T. Wang and K. Yang, *Int. J. Hydrogen Energy*, 2014, **39**, 13596–13602.

23 H. Cheng, X. Deng, S. Li, W. Chen, D. Chen and K. Yang, *Int. J. Hydrogen Energy*, 2007, **32**, 3046–3053.

24 Q. Pan, H. Shen, X. Han, J. Zhu, Z. Li, T. Pan, L. Xu and L. Lv, *RSC Adv.*, 2025, **15**, 17153–17163.

25 T. Cheng, J. Huang, W. Fang, L. He, X. Duan, G. Zou, X. Li and X. Ren, *Crystals*, 2025, **15**, 297.

26 T. Huang, J. Han, Y. Zhang, J. Yu, G. Sun, H. Ren and X. Yuan, *J. Power Sources*, 2011, **196**, 9585–9589.

27 S. E. Hsu, M. T. Yeh, I. C. Hsu, J. Y. Wang and V. Beibutian, *J. Alloys Compd.*, 1999, **293–295**, 658–662.

28 V. A. Yartys and M. V. Lototskyy, *J. Alloys Compd.*, 2022, **916**, 165219.

29 B. Ni, J. Zhu, G. Yang, L. Xu, H. Leng, W. Liu, T. Pan, X. Han and L. Lv, *Prog. Nat. Sci.*, 2024, **34**, 304–313.

30 C. E. Lundin, F. E. Lynch and C. B. Magee, *J. Alloys Compd.*, 1977, **56**, 19–37.

31 G. Sandrock, *J. Alloys Compd.*, 1999, **293–295**, 877–888.

32 R. Yamagishi, T. Kojima, S. Kameoka, D. Okuyama, T. J. Sato, C. Nishimura and A.-P. Tsai, *Int. J. Hydrogen Energy*, 2017, **42**, 21832–21840.

33 C.-N. Park, S. Luo and T. B. Flanagan, *J. Alloys Compd.*, 2004, **384**, 203–207.

34 K.-C. Chou and K. Xu, *Intermetallics*, 2007, **15**, 767–777.

35 W. Jiang, C. He, X. Yang, X. Xiao, L. Ouyang and M. Zhu, *Renewable Energy*, 2022, **197**, 564–573.

36 S. L. Li, P. Wang, W. Chen, G. Luo, X. B. Han, D. M. Chen and K. Yang, *Int. J. Hydrogen Energy*, 2010, **35**, 12391–12397.

37 Z. Cao, L. Ouyang, H. Wang, J. Liu, D. Sun, Q. Zhang and M. Zhu, *Int. J. Hydrogen Energy*, 2015, **40**, 2717–2728.

38 X. Chen, J. Xu, W. Zhang, S. Zhu, N. Zhang, D. Ke, J. Liu, K. Yan and H. Cheng, *Int. J. Hydrogen Energy*, 2021, **46**, 21973–21983.

39 A. Verma, K. Biswas, C. S. Tiwary, A. K. Mondal and K. Chattopadhyay, *Metall. Mater. Trans. A-Phys. Metall. Mater. Sci.*, 2010, **42**, 1127–1137.

40 K. Young, T. Ouchi and M. A. Fetcenko, *J. Alloys Compd.*, 2009, **480**, 428–433.